



RESEARCH ARTICLE | DECEMBER 05 2022

Copper tungsten oxide (Cu_xWO_y) thin films for optical and photoelectrochemical applications deposited by reactive high power impulse magnetron co-sputtering

A. Hrubantova ; R. Hippler  ; H. Wulff ; M. Cada ; O. Gedeon ; P. Jiricek ; J. Houdkova ; J. Olejnicek ; N. Nepomniashchaia ; C. A. Helm ; Z. Hubicka 

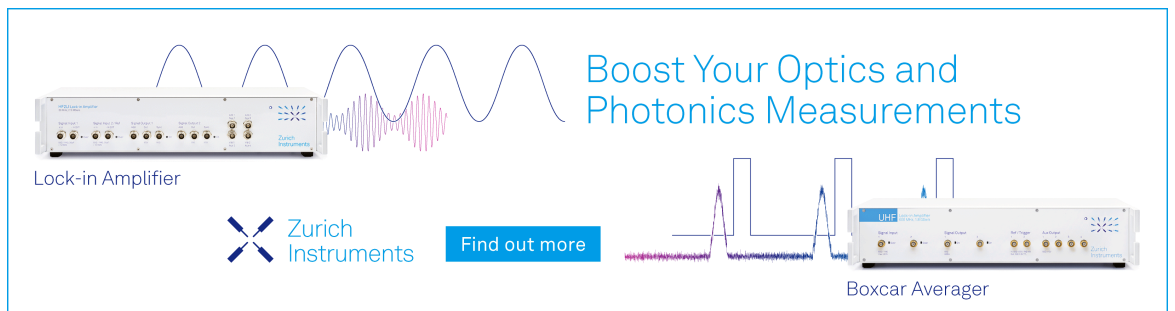
 Check for updates

J. Appl. Phys. 132, 215301 (2022)

<https://doi.org/10.1063/5.0123075>



View
Online


Export
Citation



Boost Your Optics and Photonics Measurements

Lock-in Amplifier

 Zurich Instruments

[Find out more](#)

Boxcar Averager

Copper tungsten oxide (Cu_xWO_y) thin films for optical and photoelectrochemical applications deposited by reactive high power impulse magnetron co-sputtering

Cite as: J. Appl. Phys. **132**, 215301 (2022); doi: [10.1063/5.0123075](https://doi.org/10.1063/5.0123075)

Submitted: 28 August 2022 · Accepted: 8 November 2022 ·

Published Online: 5 December 2022



View Online



Export Citation



CrossMark

A. Hrubantova,^{1,2} R. Hippler,^{1,3,a)} H. Wulff,³ M. Cada,¹ O. Gedeon,⁴ P. Jiricek,¹ J. Houdkova,¹
J. Olejnicek,¹ N. Nepomniashchaia,^{1,5} C. A. Helm,³ and Z. Hubicka¹

AFFILIATIONS

¹Institute of Physics, Czech Academy of Sciences, Na Slovance 2, 18221 Prague 8, Czech Republic

²Joint Laboratory of Optics, Palacky University in Olomouc, 17. listopadu 1192/12, 77900 Olomouc, Czech Republic

³Institut für Physik, Universität Greifswald, Felix-Hausdorff-Str. 6, 17489 Greifswald, Germany

⁴Faculty of Chemical Technology, University of Chemistry and Technology, Technická 5, 16628 Prague 6, Czech Republic

⁵Faculty of Nuclear Sciences and Physical Engineering, Czech Technical University in Prague, Brehova 7, 11519 Prague 1, Czech Republic

a) Author to whom correspondence should be addressed: hippler@physik.uni-greifswald.de

ABSTRACT

Copper tungsten oxide films are deposited with the help of reactive high power impulse magnetron sputtering (HiPIMS) in an argon/oxygen gas mixture. Two magnetrons, one equipped with a tungsten target and the other with a copper target, are employed. The HiPIMS discharge is operated with a repetition frequency of $f = 100$ Hz. Pulse widths of 100 and 20 μs separated by 25 μs are chosen for the tungsten and copper target, respectively. Films deposited on two different glass substrates [soda lime glass and fluorine doped tin oxide (FTO) coated glass] are characterized by energy dispersive x-ray spectroscopy, x-ray photoelectron spectroscopy, x-ray diffraction, Raman spectroscopy, and ellipsometry. Photoelectrochemical activity was investigated by linear voltammetry. The composition and crystal structure of as-deposited and annealed films are found to depend on the deposition conditions. Annealed films deposited on FTO glass are composed of WO_3 and CuWO_4 or Cu_2WO_4 crystal phases. Films deposited on soda lime glass are subject to sodium diffusion into the films during annealing and the formation of $\text{Na}_2\text{W}_2\text{O}_7$ and $\text{Na}_2\text{W}_4\text{O}_{13}$ phases.

© 2022 Author(s). All article content, except where otherwise noted, is licensed under a Creative Commons Attribution (CC BY) license (<http://creativecommons.org/licenses/by/4.0/>). <https://doi.org/10.1063/5.0123075>

I. INTRODUCTION

Semiconducting metal oxides are attractive materials for sensors, light absorbers, and as catalysts in photoelectrochemical (PEC) processes with applications in solar fuel production and as water splitting or CO_2 reduction devices.^{1–4} Photoanodes made of n-type binary transition metal oxide materials, such as TiO_2 , Fe_2O_3 , and WO_3 , or photocathodes of p-type CuO and Cu_2O have received much attention.¹ TiO_2 is a low cost, biocompatible, and eco-friendly compound. It has a wide bandgap of typically 3.2 eV, which limits

the usable photon spectrum to less than 4% of the incident solar radiation.^{5,6} Other metal oxides, in particular, hematite iron oxide ($\alpha\text{-Fe}_2\text{O}_3$) and amorphous tungsten trioxide (WO_3), have smaller bandgaps that are closer to the optimum bandgap of 1.8 eV for solar energy applications.^{7–9} Iron oxide, despite its nearly ideal bandgap of about 2.1 eV,^{10,11} has the disadvantage of poor electrical conductivity hindering its use in PEC applications.¹² The bandgap of WO_3 depends on the deposition conditions and its crystalline phase. Indirect bandgaps of 2.6 and 3.4 eV have been reported for amorphous and crystalline WO_3 films, respectively.^{13–15} In combination

24 April 2024 14:10:26

with other elements, the bandgap of WO_3 can be reduced further. Nitrogen-doping during film deposition reduces the WO_3 bandgap to 2.43 eV.¹³ An admixture of CdTe to WO_3 narrows the bandgap to 2.47 eV.¹⁶ Amorphous copper tungsten oxides with variable Cu/W ratios of 0.33, 1.1, and 2.5 and with bandgaps of 2.63, 2.05, and 1.88 eV, respectively, have been reported.¹⁷ Recently, due to its small bandgap of 2.3 eV and its excellent chemical stability in aqueous solutions, copper tungstate (CuWO_4) has emerged as an interesting photoanode candidate for water-splitting devices and as a catalyst.^{1,18–21} Comparatively little is yet known about other copper tungstates, e.g., Cu_3WO_6 of bivalent Cu(II) atoms and Cu_2WO_4 of monovalent Cu(I) atoms, which requires further investigations.^{22–25}

Magnetron sputtering is a commercially employed technique for large area deposition of, e.g., architectural glass. High power impulse magnetron sputtering (HiPIMS) has emerged as a promising tool for deposition of functional films.^{26–31} A HiPIMS discharge generates large plasma densities together with high ion energies, which influence the properties of deposited films. Magnetron co-sputtering using two (or more) cathodes is used for the deposition of binary and, in combination with reactive gases, ternary compounds. Reactive co-sputtering in a reactive, e.g., argon + oxygen gas mixture is a flexible technique allowing for the deposition of thin films with a variable composition. As a further benefit compared to continuous (direct current) magnetron sputtering, the HiPIMS discharge is weakly influenced by a hysteresis effect caused by surface contamination with the reactive gas.^{32–34} As a disadvantage, the composition achieved by co-sputtering is difficult to predict, and a predetermined film composition is not readily possible.

The purpose of the present paper is twofold: (i) to explore the discharge conditions for deposition of ternary copper tungsten oxide films and (ii) to examine the deposited films with respect to morphology, bond structure, optical properties, and photoelectrochemical activity. Copper tungsten oxide films are deposited with copper and tungsten cathodes of a reactive dual-HiPIMS discharge in an argon/oxygen gas mixture. The Cu/W ratio of the film is varied by changing the discharge voltage and current supplied to the Cu cathode (without changing the voltage at the W cathode). In addition, the influence of gas pressure on film properties is investigated. Films are deposited on two different substrate materials, i.e., soda lime glass and fluorine-doped tin oxide (FTO)-covered glass. As expected, deposited films are amorphous, and post-deposition annealing has been applied to the films. Annealing not only changes the crystallographic structure but, in general, leads to more dense films with lower defect concentrations. In addition, as was noted during the investigations, annealing leads to diffusion of sodium atoms into the annealed film and to the formation of sodium tungstates when the soda lime glass substrate is used. As-deposited and annealed films are characterized by various means, in particular, secondary electron microscopy (SEM), grazing incidence x-ray diffractometry (GIXRD), and Raman spectroscopy. The optical and photoelectrochemical functionality of as-deposited and annealed copper tungstate films is investigated. Optical properties are examined by means of UV-VIS and spectroscopic ellipsometry. Photoelectrochemical activity and the suitability of the deposited films for, e.g., water-splitting applications is examined by means of voltammetry measurements.

II. EXPERIMENT

The experimental setup has been briefly described before.³⁵ A plasma chamber with a volume of 30 l is evacuated by a turbomolecular pump (Leybold, Turbovac MAG W300, with a nominal pumping speed of 300 l/s for N_2) together with a rotary vane backing pump (pumping speed 25 m^3/h). The achieved base pressure is 1×10^{-4} Pa. Two planar unbalanced magnetrons, one equipped with a tungsten and one equipped with a copper target (diameter 50.8 mm, nominal thickness 6 mm, purity 99.95%), are employed. The two cathodes are confocally aligned toward the center of the substrate holder. Argon (purity 99.999%) and oxygen gas (purity 99.995%) are separately admitted to the vacuum chamber with the help of two gas flow controllers. The argon and oxygen flow rates are set to 26 and 78 sccm, respectively. The gas pressure is measured with a capacitance vacuum gauge. Both magnetrons are powered by DC power supplies that are operated in a voltage regulation mode. Pulsed magnetron sputtering operation is achieved with the help of a home-built dual power switch delivering two negative high voltage pulses during the discharge.^{36–40} The power switch is controlled with the help of a two-channel arbitrary waveform generator (Agilent 33250A) delivering two pulses, one with a width of 100 μs , which, after a delay of 25 μs , is followed by a second pulse with a width of 20 μs . The repetition frequency (period) is set to $f = 100$ Hz ($t_p = 10$ ms). The voltage and current waveforms are simultaneously recorded using voltage (Textronix P5100A) and current probes (Textronix A622) connected to a four-channel digital storage oscilloscope (Agilent DSO 7104B).

The measured voltage and current waveforms of the dual-HiPIMS discharge are displayed in Fig. 1. Initial discharge voltages of -1020 and -540 V are applied to the W and Cu cathodes, respectively. After ignition, the voltage applied to the W cathode within the first 10 μs reduces to -900 V; it gradually increases to -990 V toward the end of the pulse. The discharge current at the W cathode increases to 12 A within 19 μs after ignition; it decreases to 4.5 A within the next 30 μs and remains approximately constant for the remaining 50 μs until the end of the pulse. The Cu discharge is ignited 25 μs after the termination of the W discharge. The initial discharge voltage applied to the Cu cathode is -540 V; it gradually decreases to -430 V during the next 20 μs until the applied voltage is terminated. The Cu discharge shows an ignition delay of about 3 μs ; it reaches a discharge current of 45 A within the next 15 μs until the end of the pulse.

The films are deposited either on microscope slides made from soda lime glass (MG) or on fluorine-doped tin oxide-coated (FTO) glass substrates with a size of 25×50 mm^2 . Depositions are carried out at gas pressures of 1.2 Pa (films CuWO-A, CuWO-B, and CuWO-C), 2.4 Pa (film CuWO-D), and 3.6 Pa (film CuWO-E); see Table I. Both substrates are mounted together on a floating substrate holder (diameter 8 cm) rotating at a speed of 1 revolution/min. The distance between the target surface and the substrate holder is 15 cm. The deposition times are 60–120 min. Deposited films are annealed in air at a temperature of 450 °C. The tempering cycle consists of a heating phase with a heating rate of 5 °C/min (≈ 85 min), a tempering phase of 4 h at 450 °C, and a cooling-down phase of 12 h or more. Deposited samples are cut into small pieces of typically 10×25 mm^2 for further analysis.

24 April 2024 14:10:26

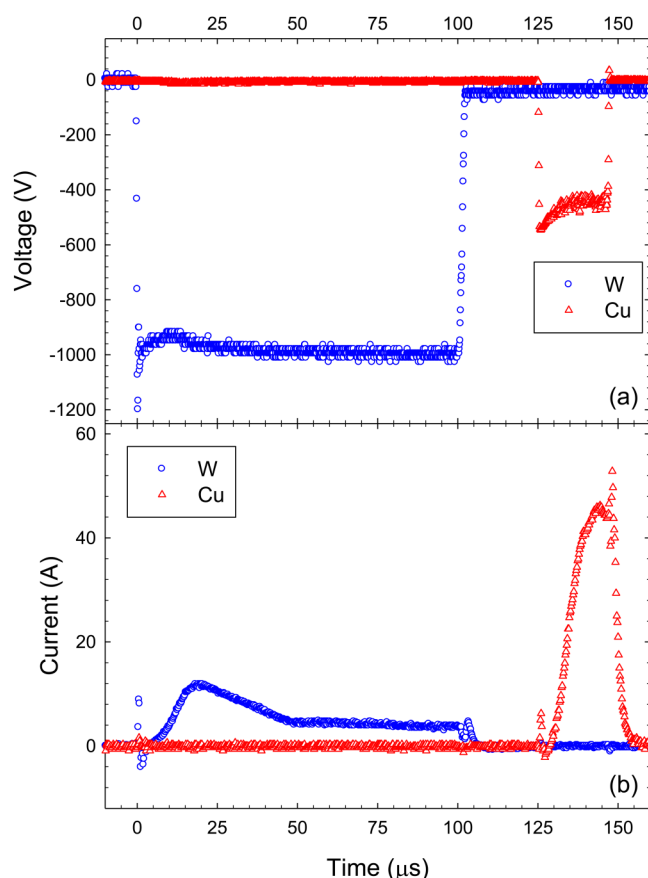


FIG. 1. (a) Discharge voltage and (b) discharge current vs time. The dual-HiPIMS discharge was operated with initial voltages of -1020 and -540 V and pulse lengths of 100 and 20 μs at the W and Cu cathodes, respectively. Argon flow rate 26 sccm, oxygen gas flow rate 78 sccm, and gas pressure $p = 1.2$ Pa.

Deposition conditions, in particular, energy per pulse, gas pressure during deposition, and deposition time of the different films, are summarized in Table I.

The film thickness is determined by surface profilometry (Alpha Step 500, Tencor). The surface morphology is investigated by scanning electron microscopy (FEI Quanta 3D, FEI, USA). The film composition is measured using energy dispersive x-ray spectroscopy (EDX) with a Tescan LYRA 3 microscope equipped with a Bruker Xflash 10-6 x-ray detector. The incident electron energy is set to 5 keV.

Films are characterized by x-ray photoelectron spectroscopy (XPS). Photoelectron spectra are measured with an AXIS Supra photoelectron spectrometer (Kratos Analytical Ltd., UK) using monochromatized Al- $K\alpha$ radiation with a photon energy of 1486.6 eV. High-resolution spectra are recorded with a pass energy of 10 eV and with steps of 0.1 eV, resulting in an overall energy resolution of 0.45 eV (full width at half maximum) as determined with the Ag $3d_{5/2}$ line.⁴⁰

TABLE I. Energy per pulse supplied to W and Cu cathodes, the corresponding W/Cu pulse energy ratio, gas pressure p , deposition time t , film thickness d , and photo current density j (at 1 V vs Ag/AgCl) of annealed films deposited on FTO-coated glass for a HiPIMS discharge operated with 100 and 20 μs long pulses on the W and Cu cathode, respectively.

Sample	Pulse energy (J)		Cu/W ratio	p (Pa)	t (min)	d (nm)	j ($\mu\text{A}/\text{cm}^2$)
	W	Cu					
CuWO-A	0.41	0.07	0.17	1.2	60	243	105
CuWO-B	0.54	0.26	0.48	1.2	60	295	105
CuWO-C	0.41	0.45	1.1	1.2	60	325	<1
CuWO-D	0.72	0.49	0.67	2.4	120	588	350
CuWO-E	0.70	0.50	0.72	3.6	120	460	135

Crystallographic properties are analyzed using x-ray diffraction (XRD) recorded in grazing incidence geometry with an incidence angle $\omega = 1^\circ$. An Empyrean diffractometer (Malvern Panalytical) using Cu $K\alpha$ radiation ($\lambda = 0.154$ nm) in the 2θ range 10° – 100° with a step size of 0.02° is employed. XRD analysis is performed with a HighScore Plus 4.0 software package (Malvern Panalytical). Raman spectra are taken at room temperature using a Renishaw Raman Microscope RM 1000 with a polarized beam of an Ar⁺ ion laser ($\lambda = 514.5$ nm) in the back-scattering configuration. Transmittance spectra of deposited films are measured with a spectrophotometer (LAMBDA 1050 UV/Vis/NIR, Perkin-Elmer).

Spectroscopic ellipsometry is conducted at room temperature (300 K) in a dry nitrogen atmosphere with a variable angle ellipsometer (J.A. Woollam VUV-VASE) in the photon energy range of 0.8 – 6.5 eV. The measurements are made at three angles of light incidence (60° , 65° , and 70°) with a typical step size of 0.04 eV. The refractive index n , extinction coefficient k , and absorption coefficient α are obtained with the help of the commercial WVASE software. The employed ellipsometric model of the samples consists of a substrate layer, a film layer, and a surface roughness layer. At first, ellipsometric measurements of the substrates are made, and their optical constants are determined using a combination of Cody-Lorentz and Lorentz oscillators. Next, the substrates' optical constants are added to the model for the films. The optical constants of the film layer are defined using Gaussian oscillators. A possible dispersion in the dielectric function created by absorption outside of the studied range is simulated by a zero-width oscillator (a pole). Inhomogeneity along the film's thickness is simulated by a gradient of optical constants included in the model as a series of homogenous layers with optical constants slightly changing in each layer. The surface roughness layer is modeled as a mixture of 50% of the film's material and 50% voids according to the Bruggeman effective medium approximation. Applicability of the model fit to the experimental data is evaluated based on a standard ellipsometric MSE parameter, which characterizes the difference between modeled and experimental data. The obtained MSE values are in the range of 1.5 – 6.5 depending on the sample and are deemed satisfactory.

The resistivity of the deposited films on soda lime glass substrates is investigated using the van der Pauw method.⁴¹ The

24 April 2024 14:10:26

electrical current is supplied by a Keithley 6487 picoammeter/voltage source, and voltage measurements are taken using a Keithley 6517B electrometer/high resistance meter.

Photoelectrochemical properties are investigated by linear sweep voltammetry (LV). Measurements are carried out in an electrochemical cell using a three-electrode configuration in a $0.1 \text{ mol l}^{-1} \text{ Na}_2\text{SO}_4$ (Penta Chemicals) electrolyte and under simulated solar light irradiation employing an AM1.5G filter and a Xe lamp (Hamamatsu C4251) with an intensity of 62 mW/cm^2 . The cell is equipped with a quartz window; the irradiated surface area is 1 cm^2 . The deposited thin film on FTO-coated glass serves as a working electrode (WE) and a platinum sheet ($1 \times 1 \text{ cm}^2$) as a counter electrode (CE). As a reference electrode (REF), we use an Ag/AgCl electrode (sat. KCl, +197 mV vs SHE, pH electrode Theta 90). The electrodes are connected to a potentiostat (OGF 500, Origaflex) in a three-electrode configuration.

III. RESULTS AND DISCUSSION

A. Film composition and bond structure

The film composition as obtained from the EDX measurements is shown in Table II. The oxygen content of the films is in the range of 75%–80% except for film CuWO-C where it is 62% and 64% for the as-deposited and annealed films, respectively. The oxygen content is, hence, close to the values of fully oxidized tungsten trioxide (WO_3), which, as we shall see below, constitutes a major part of the films. The smaller oxygen content of the CuWO-C film is readily explained by the larger Cu content in the film and the smaller ability of copper tungstate (CuWO_4) to bind oxygen.

The Cu/W composition ratio as a function of the Cu/W pulse energy ratio is shown in Fig. 2. As expected, the Cu/W composition ratio increases when the Cu/W pulse energy ratio is increased. Results for the as-deposited films are about $1.6\times$ larger compared to the annealed films. The smaller Cu composition may be explained by a reduced detection probability caused by the diffusion of copper atoms from the surface into the bulk of the film,^{42,43} which is supported by our ellipsometry measurements (see below). A simple estimate based on the penetration depth of the employed primary electrons in WO_3 ⁴⁴ yields 158 nm, which is much shorter than the film thickness. In addition, Cu-L x rays in comparison with W-M experience stronger absorption in the film due to the

TABLE II. Composition (atom %) of as-deposited and annealed films on FTO glass and the corresponding Cu/W ratio.

Sample	As-deposited			Annealed				
	W (%)	Cu (%)	O (%)	Cu/W	W (%)	Cu (%)	O (%)	Cu/W
CuWO-A	17.9	4.2	77.8	0.234	18.5	2.7	78.8	0.146
CuWO-B	16.9	5.7	77.4	0.339	19.2	3.6	77.2	0.188
CuWO-C	10.0	28.6	61.5	2.86	11.5	24.5	64.0	2.130
CuWO-D	16.1	8.8	75.1	0.547	19.5	3.7	76.9	0.190
CuWO-E	16.7	7.5	75.8	0.449	16.4	6.2	77.4	0.378

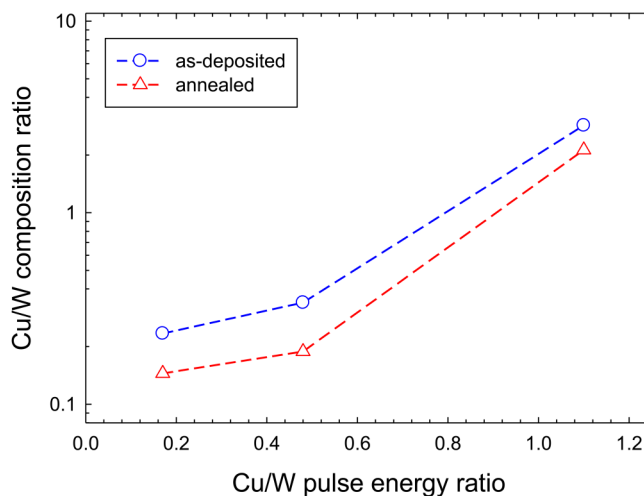


FIG. 2. Cu/W composition ratio vs Cu/W pulse energy ratio of as-deposited and annealed CuWO-A, CuWO-B, and CuWO-C thin films on FTO glass substrates. Gas pressure during deposition 1.2 Pa.

smaller x-ray energy (0.93 vs 1.78 keV), which reduces the detection probability the further away the copper atoms are from the surface.

As an example, the annealed CuWO-D film was investigated by x-ray photoelectron spectroscopy (XPS). Figure 3 displays the high-resolution Cu-2p, W-4f, and O-1s photoelectron lines. The result indicates the presence of Cu, W, and O in the film. Similar spectra were reported by Tang *et al.*⁴⁵ The small Cu count rate is due to the small copper content of the film ($\text{Cu/W} = 0.19$; see Table II). The Cu/W ratio extracted from the XPS data is 0.17, which compares favorably with the EDX results. Nevertheless, we would like to point out that XPS is a surface-sensitive technique with a typical information depth of 1 nm, and a comparison with EDX results has some limitations.

Deconvolution of photoelectron lines into several sub-peaks associated with certain chemical compounds provides information related to the possible chemical bonds of the investigated elements. Figure 3(a) shows the tungsten W-4f_{7/2}, W-4f_{5/2}, and W-5p_{3/2} lines at 35.8, 38.0, and 41.6 eV, respectively. The energetic position of the lines is about 4.6 eV larger than expected for metallic W lines. This is attributed to the oxidation and the formation of WO_6 octahedrons of the fully oxidized WO_3 and/or CuWO_4 crystal structure.

Figure 3(b) shows de-convolution of the copper Cu-2p_{3/2} photoelectron spectrum into Cu_2O and CuO components at 932.6 and 934.9 eV. In addition, we observe a pronounced shake-up satellite peak, which can be decomposed into at least two sub-peaks centered at 941.1 and 943.8 eV. Satellite peaks are well known and an indication of oxidized Cu(II) species, e.g., Cu(II)O or Cu(II)(OH)₂.^{46,47} The presence of Cu_2O may indicate that a minor fraction of Cu is only partly oxidized.

Figure 3(c) shows the deconvolution of the oxygen O-1s_{1/2} photoelectron spectrum with a main sub-peak at 530.8 eV and a

24 April 2024 14:10:26

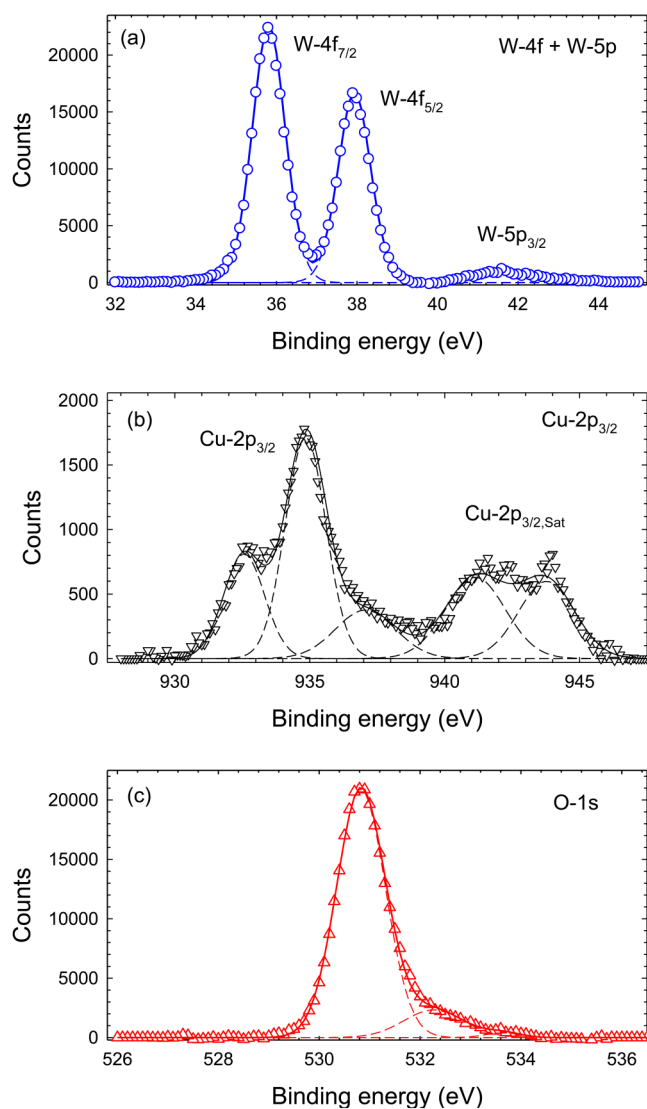


FIG. 3. X-ray photoelectron spectra of an annealed CuWO-D film on FTO-coated glass substrate. (a) W-4f and W-5p, (b) Cu-2p_{3/2}, and (c) O-1s_{1/2}.

smaller sub-peak at 532.3 eV. These sub-peaks are attributed to fully or partly oxidized metal atoms.⁴⁸ A tiny sub-peak that appears at 533.7 eV is attributed to oxygen absorbed on the surface, e.g., absorbed water molecules.

B. Film morphology and crystal structure

Figure 4 show top and cross-sectional scanning electron micrographs (SEMs) of the annealed CuWO-C, CuWO-D, or CuWO-E films deposited on FTO-coated glass at gas pressures of 1.2, 2.4, or 3.6 Pa, respectively. All films display small surface structures with typical sizes in the 20–300 nm range. Cross-sectional

views show the deposited films on top of the FTO layer. Derived film thicknesses of 325, 614, and 500 nm for films CuWO-C, CuWO-D, and CuWO-E, respectively, are in fair agreement with the profilometry measurements (Table I). The derived deposition rates are 325, 307, and 250 nm/h taking the different deposition times of 1 or 2 h into account. It, thus, appears that the deposition rate decreases with increasing gas pressure.

The surface of film CuWO-C shows near-spherical grain-like structures with sizes in the range of 50–100 nm and several elongated rod-like structures with a typical length of 250 nm, which are eventually formed by clustering of the smaller structures. Some very large structures with sizes in the 500 nm range are also observed. Film CuWO-D shows clearly separated small grains in the 20–40 nm range, some of which form larger crystal-like structures with sizes in the range of 100–250 nm. The film was deposited at a twice as large pressure (2.4 Pa) compared to film CuWO-C. According to the structure-zone diagram,⁶⁸ structural properties of deposited films depend on the kinetic energy of impinging ions during film growth. It is known that the kinetic energy of plasma ions is reduced when the gas pressure increases.⁶⁹ A smaller kinetic energy of impinging ions during film growth, hence, should result in less compact and porous films, as is observed here. The surface of film CuWO-E shows large non-spherical crystallites in the 150–350 nm size range eventually formed by clustering of small grains (20–40 nm), some of which are noticeable in the space between the larger crystallites.

Deposited Cu_xWO_y films are investigated by grazing incidence x-ray diffraction (GIXRD). Figure 5 shows results for as-deposited films deposited on microscope glass (CuWO-A-MG) or FTO-coated glass (CuWO-B-FTO and CuWO-C-FTO) substrates. The narrow GIXRD reflections observed for the films deposited on FTO-coated glass originate from the crystalline tin oxide layer of the substrate, which has a preferred [200] orientation, as confirmed by XRD measurements in Bragg–Brentano geometry. All samples exhibit diffractograms with two broad peaks at 26° and 52°. A similar diffractogram was reported by Abe *et al.*⁴⁹ for deposition of tungsten oxide films.

GIXRD diffractograms of annealed films are displayed in Figs. 6 and 7 and summarized in Table III. A quantitative Rietveld analysis has been carried out for the annealed samples. The fractions indicated in Table III are estimated from the Rietveld results. Figure 6 shows the results for annealed films on FTO-coated glass substrates. Films CuWO-A and CuWO-B contain the monoclinic WO₃ crystalline phase. These films are largely composed of O and W (Table I), and the large WO₃ component appears reasonable. In addition, the CuWO-A film contains a minor CuWO₄ phase, which contributes about 10%. The CuWO₄ phase is readily identified by the two peaks at 15.3° and 19.0°, which are absent for WO₃. Films CuWO-D and CuWO-E contain the monoclinic WO₃ phase plus a 3× and 9×, respectively, smaller CuWO₄ phase.

The diffractogram of the annealed CuWO-C film on FTO-coated glass substrates shows a small contribution from CuWO₄. Reflections from the FTO layer are also visible. The main contribution is a yet unknown crystalline phase, which gives rise to strong reflections at 13.13°, 15.17°, 24.50°, 25.11°, 26.37°, 33.45°, 38.41°, and 40.00°. The unknown phase resembles a monoclinic lattice with lattice parameters $a = 0.809$ nm, $b = 1.350$ nm,

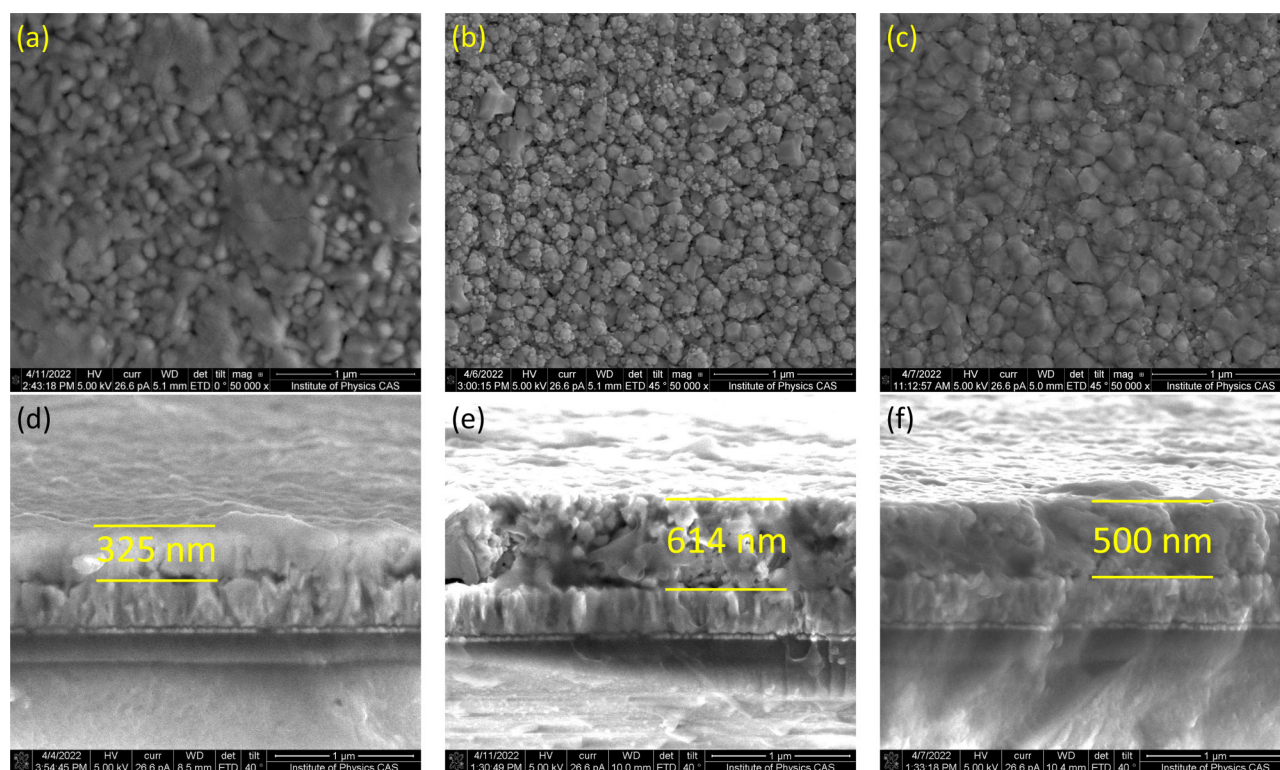


FIG. 4. Scanning electron micrographs of annealed films deposited on FTO-coated glass. Top views of (a) CuWO-C, (b) CuWO-D, and (c) CuWO-E films and cross-sectional views of (d) CuWO-C, (e) CuWO-D, and (f) CuWO-E films deposited at gas pressures of 1.2, 2.4, and 3.6 Pa, respectively.

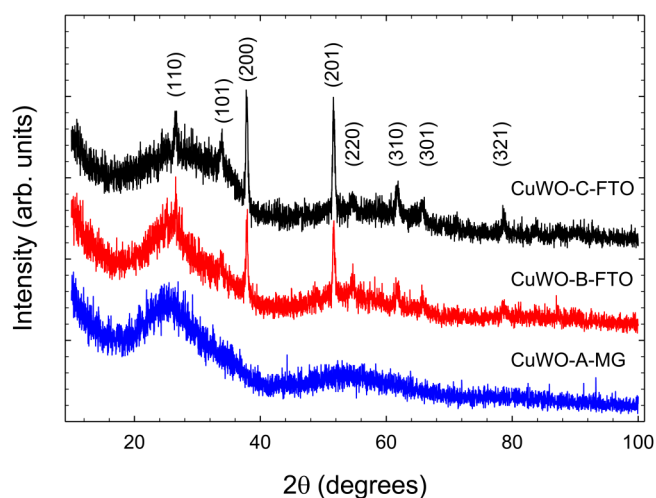


FIG. 5. GIXRD diffractogram of as-deposited Cu_xWO_y films on MG or FTO-coated glass substrates. In order to ease comparison, some diffractograms have been shifted upward. Peaks originating from the FTO layer are labeled.

$c = 1.004 \text{ nm}$, and $\beta = 110.4^\circ$. A Rietveld analysis was employed to check that the positions of additional peaks match the unit cell parameters of the compound. The film has a large Cu/W ratio of more than 2; see Table II. Several copper tungstates with a large Cu/W ratio have been reported in the literature. Cu_3WO_6 , together with CuWO_4 , is part of the CuO-WO_3 system of bivalent Cu(II) atoms.²² On the other hand, Cu_2WO_4 is part of the $\text{Cu}_2\text{O-WO}_3$ system of monovalent Cu(I) atoms.^{23,24} We believe that the newly observed phase is a new modification of Cu_2WO_4 as Cu_3WO_6 (and CuWO_4) can be ruled out. Unlike the previously reported triclinic Cu_2WO_4 phases, the new phase has a monoclinic lattice.

Annealed films deposited on MG glass are affected by sodium diffusion from the glass substrate into the deposited film during annealing. The GIXRD results for these films are displayed in Fig. 7 and summarized in Table III. Accordingly, film CuWO-A consists of a single $\text{Na}_2\text{W}_2\text{O}_7$ phase. Other crystalline phases are not observed for this film. Film CuWO-B is composed of two crystalline phases: $\text{Na}_2\text{W}_4\text{O}_{13}$ and weak $\text{Na}_2\text{W}_2\text{O}_7$. The (100) and (200) planes of $\text{Na}_2\text{W}_4\text{O}_{13}$ are responsible for the strong reflection at 10.8° and 21.8° . Film CuWO-C appears to be unaffected by sodium diffusion. This film has the largest Cu content, which, eventually, suppresses Na diffusion into the film during annealing.

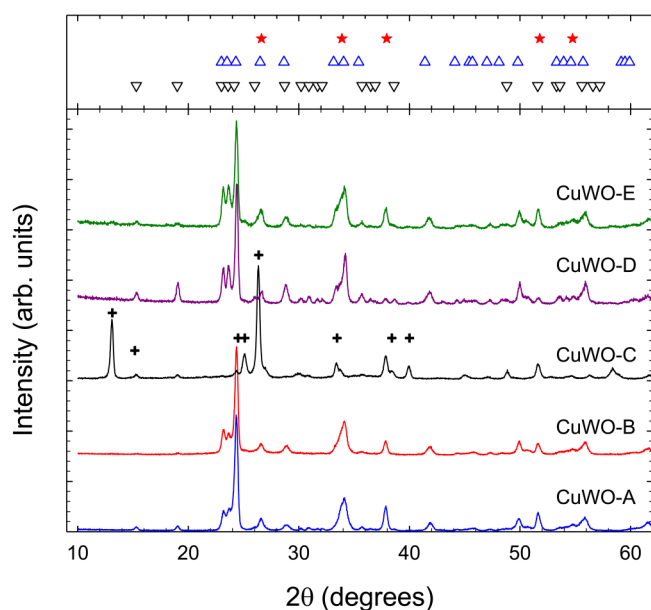


FIG. 6. GIXRD diffractogram of annealed Cu_xWO_y films deposited by HiPIMS on FTO-coated glass substrates. Reflections from the assumed monoclinic Cu_2WO_4 (+), monoclinic WO_3 (Δ), CuWO_4 (∇), and FTO (\star) are indicated.

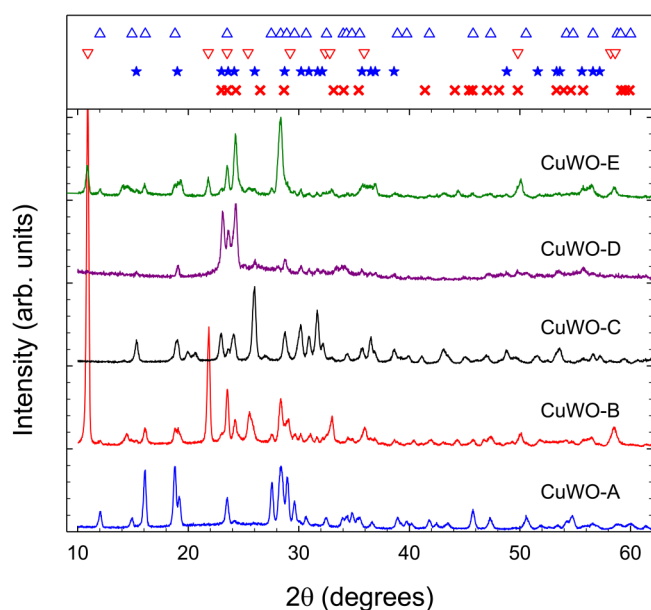


FIG. 7. GIXRD diffractogram of annealed Cu_xWO_y films deposited by HiPIMS on MG substrates. Reflections from $\text{Na}_2\text{W}_2\text{O}_7$ (Δ), $\text{Na}_2\text{W}_4\text{O}_{13}$ (∇), CuWO_4 (\star), and monoclinic WO_3 (\times) are indicated.

TABLE III. Main crystallographic phases of annealed films on microscope glass (MG) and FTO-coated glass as obtained from the GIXRD measurements. Fractions of minor phases are given in parentheses.

Sample	MG	FTO
CuWO-A	$\text{Na}_2\text{W}_2\text{O}_7$	$\text{WO}_3 + \text{CuWO}_4$ (10%)
CuWO-B	$\text{Na}_2\text{W}_4\text{O}_{13} + \text{Na}_2\text{W}_2\text{O}_7$ (15%)	WO_3
CuWO-C	CuWO_4	Cu_2WO_4 + CuWO_4 (8%)
CuWO-D	$\text{WO}_3 + \text{CuWO}_4$ (50%)	$\text{WO}_3 + \text{CuWO}_4$ (25%)
CuWO-E	$\text{Na}_2\text{W}_2\text{O}_7 + \text{Na}_2\text{W}_4\text{O}_{13}$ (46%) + CuWO_4 (8%)	$\text{WO}_3 + \text{CuWO}_4$ (10%)

The crystalline part of the film is composed of CuWO_4 . The influence of gas pressure on the structural properties of the deposited films was investigated for films CuWO-D and CuWO-E, which were deposited at pressures of 2.4 and 3.6 Pa, respectively. Film CuWO-D appears to be unaffected by Na diffusion, which may be explained by its larger film thickness and the longer time that Na atoms need to reach the top (near-surface) part of the film. The film shows a monoclinic WO_3 and CuWO_4 phase. Film CuWO-E is significantly thinner compared to film CuWO-D; it shows $\text{Na}_2\text{W}_2\text{O}_7$ and $\text{Na}_2\text{W}_4\text{O}_{13}$ phases with a small CuWO_4 contribution.

The Raman spectroscopy results of Cu_xWO_y films deposited on FTO-coated glass substrates are displayed in Fig. 8. The Raman spectra of the annealed CuWO-A and CuWO-B films as well as of the not shown CuWO-D and CuWO-E films are rather similar. Raman spectra of the films show a number of phonon bands at about 65, 134, 273, 334, 714, 805, 907, and 985 cm^{-1} , including a broad structure at 1107 cm^{-1} . The main peaks at 714 cm^{-1} and 805 cm^{-1} are typical for tungsten trioxide (WO_3). For comparison, results for a WO_x film deposited with the help of a hollow cathode discharge are shown in Fig. 8 as well. The WO_3 structure is composed of distorted corner-shared WO_6 octahedra. The major vibrational modes at 805, 714, and 273 cm^{-1} are assigned to W–O stretching, W–O bending, and W–O–W deformation modes, respectively.⁵⁰ Other bands at 65 and 134 cm^{-1} are assigned to vibrational modes of $(\text{W}_2\text{O}_2)_n$ chains of the WO_3 lattice. A small peak at 907 cm^{-1} is associated with CuWO_4 . The present results, hence, indicate that films CuWO-A and CuWO-B as well as films CuWO-D and CuWO-E are largely composed of crystalline WO_3 , in contrast to film CuWO-C.

The dominating peak of film CuWO-C at 965/979 cm^{-1} is presumably due to distorted W–O bonds in combination with Cu.⁵¹ A prominent peak close to this position has been identified in calculated Raman spectra from triclinic Cu_2WO_4 but was not experimentally verified yet.²⁵ A small peak at 908 cm^{-1} is associated with CuWO_4 .^{45,52,53} The broad band in the range 545–628 cm^{-1} is attributed to Cu(I)O bonds of the Cu_2WO_4 lattice,^{54,55} which supports the GIXRD results and our interpretation of a monoclinic Cu_2WO_4 phase.

The Raman spectroscopy results of Cu_xWO_y films on MG substrates are displayed in Fig. 9. Annealing, as is known from the

24 April 2024 14:10:26

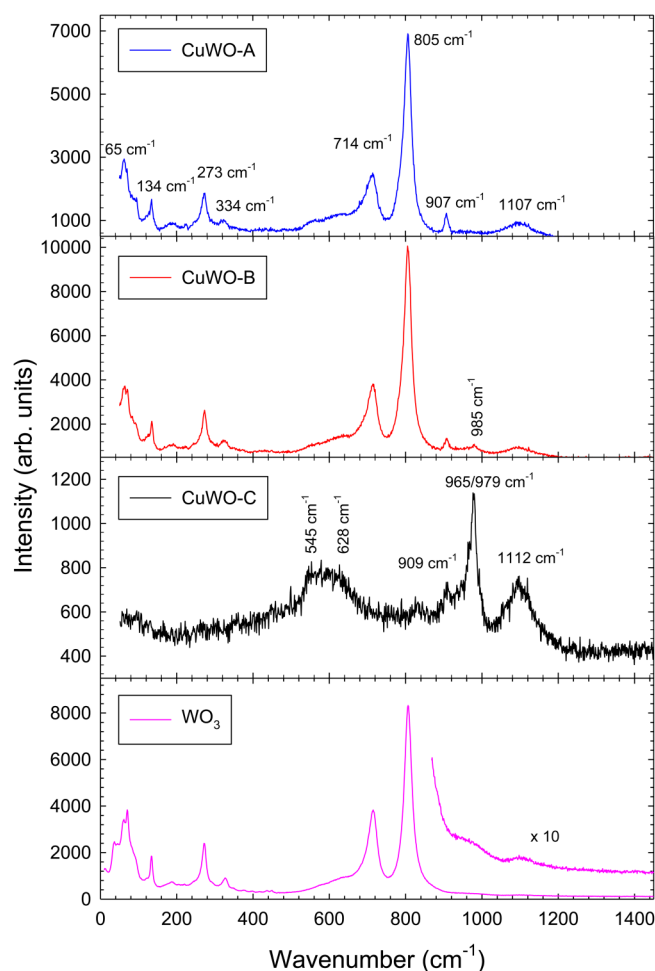


FIG. 8. Raman spectroscopy of annealed CuWO-A, CuWO-B, and CuWO-C films deposited on FTO-coated glass substrates. Also shown are results for a tungsten oxide film (WO_3).

GIXRD measurements, gives rise to Na diffusion into the films. All three spectra show a broad band at about 1110 cm^{-1} , which originates from the soda lime glass substrate.⁵⁶ Film CuWO-A having the smallest Cu/W ratio is dominated by a sharp peak at 957 cm^{-1} and a smaller peak at 938 cm^{-1} . The bands are identified as symmetric W–O stretching modes in WO_4 tetrahedra of the $\text{Na}_2\text{W}_2\text{O}_7$ crystal,^{57–59} which confirms our GIXRD results. Small peaks at 885 and 835 cm^{-1} are connected with W–O stretching in WO_4 tetrahedra and WO_6 octahedra, respectively, which are both part of the $\text{Na}_2\text{W}_2\text{O}_7$ crystal.⁵⁸

The CuWO-B film displays three strong bands at 776 cm^{-1} (with a shoulder at 795 cm^{-1}), at 908 cm^{-1} , and at 948 cm^{-1} (with a small shoulder at 954 cm^{-1}). The bands at $776/795\text{ cm}^{-1}$ are assigned to W–O stretching modes of WO_6 octahedra of $\text{Na}_2\text{W}_4\text{O}_{13}$,^{59,60} which is in agreement with the GIXRD results.

The bands at $948/954\text{ cm}^{-1}$ of the CuWO-B film are close to the positions of symmetric W–O stretching modes in WO_4

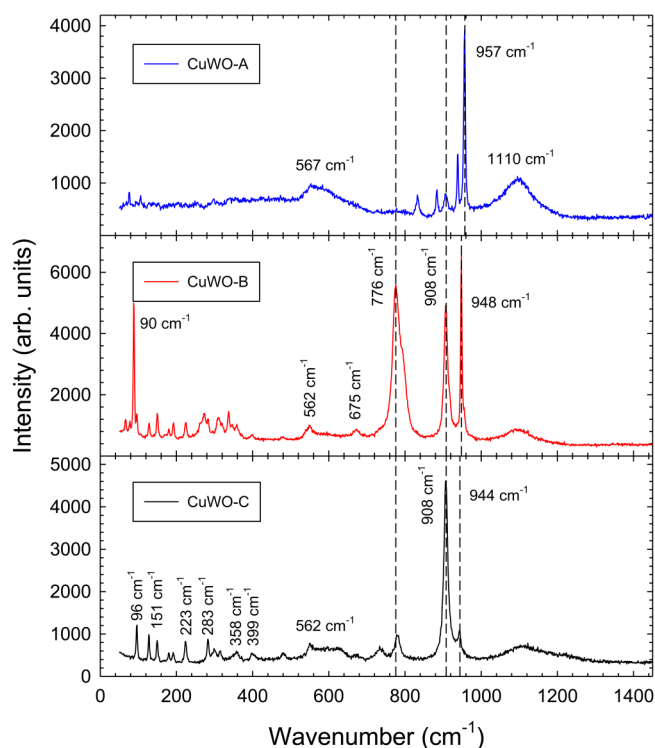


FIG. 9. Raman spectroscopy of annealed CuWO-A, CuWO-B, and CuWO-C films deposited on MG substrates.

tetrahedra, as observed for $\text{Na}_2\text{W}_2\text{O}_7$; see film CuWO-A. Kim *et al.* assigned this band to $\text{Na}_2\text{W}_4\text{O}_{13}$,⁶⁰ which, however, according to Viswanathan,⁶¹ does not form WO_4 tetrahedra. Hence, although it appears safe to assign these bands to the stretching modes of WO_4 tetrahedra of some kind of sodium tungstate, the exact origin either from $\text{Na}_2\text{W}_2\text{O}_7$ and/or from $\text{Na}_2\text{W}_4\text{O}_{13}$ remains unclear. The remaining strong band at 908 cm^{-1} indicates the presence of copper tungstate, CuWO_4 .

The CuWO-C film is dominated by a band at 908 cm^{-1} , which we associated with the formation of copper tungstate CuWO_4 .^{45,52,53,62} The band is presumably caused by symmetric stretching of W–O bonds in WO_6 .⁶² The less intense peaks at 96, 129, 151, 180, 192, 223, 283, 299, 316, 358, 399, and 781 cm^{-1} are all associated with the formation of copper tungstate CuWO_4 ,^{45,52,53,62} which confirms our GIXRD results.

C. Optical properties

The transmittance of as-deposited films CuWO-A, CuWO-B, and CuWO-C on MG glass measured with a UV–VIS spectrometer are displayed in Fig. 10. The CuWO-A and CuWO-B films become opaque for wavelength $\lambda \leq 400\text{ nm}$, which corresponds to photon energies $E_{ph} \geq 3.1\text{ eV}$. The cut-off behavior of film CuWO-C is distinctly different; the cutoff occurs at larger wavelengths (smaller photon energies) below 500 nm (2.5 eV).

24 April 2024 14:10:26

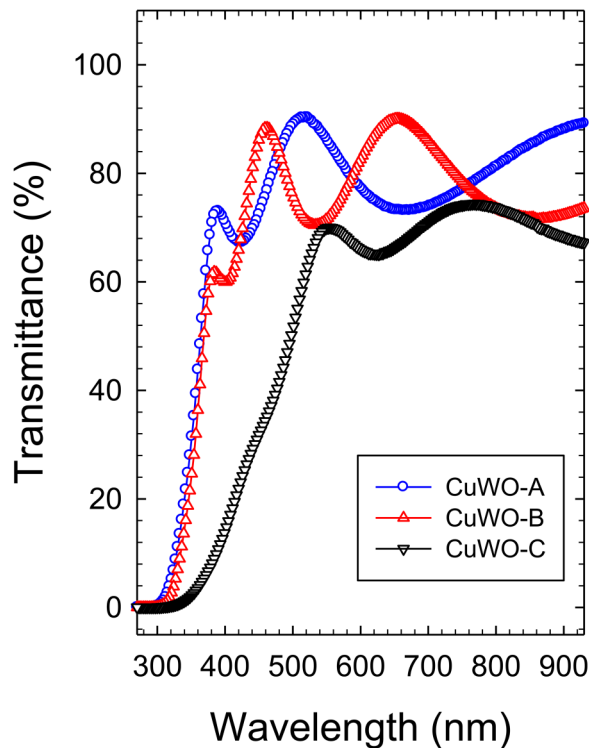


FIG. 10. Transmittance spectra of as-deposited CuWO-A (\circ), CuWO-B (Δ), and CuWO-C (∇) films on MG substrates.

The refractive index n and the extinction coefficient k as determined by ellipsometry are shown in Fig. 11. The refractive index displays weak dependence on photon energy. The extinction coefficient k displays a pronounced increase above 3 eV. In addition, a weak absorption feature is observed between 1 and 2 eV for the annealed films, whereas it is absent for the as-deposited film. It has been argued that absorption in this range arises from a dipole-forbidden inter d - d transition of Cu^{2+} ($3d^9$) cations, which does not generate mobile charge carriers.⁶³ The measured optical constants n and k are similar to the behavior of a tungsten oxide film, which is shown for comparison.

Figure 12 displays the results for the annealed CuWO-D, as-deposited CuWO-E, and annealed CuWO-E films as obtained from the ellipsometry measurements. In order to extract the optical bandgap from the ellipsometry measurements, we employ the so-called Tauc plot making use of

$$(\alpha h\nu)^r = h\nu - E_g, \quad (1)$$

where α is the absorption coefficient, $h\nu$ the photon energy, and h Planck's constant.⁶⁴ The exponent r depends on the type of bandgap: $r = 0.5$ in the case of an indirect bandgap and $r = 2$ for a direct bandgap. In the following analysis, we assume an indirect bandgap as is the case for tungsten oxide, which is an n-type

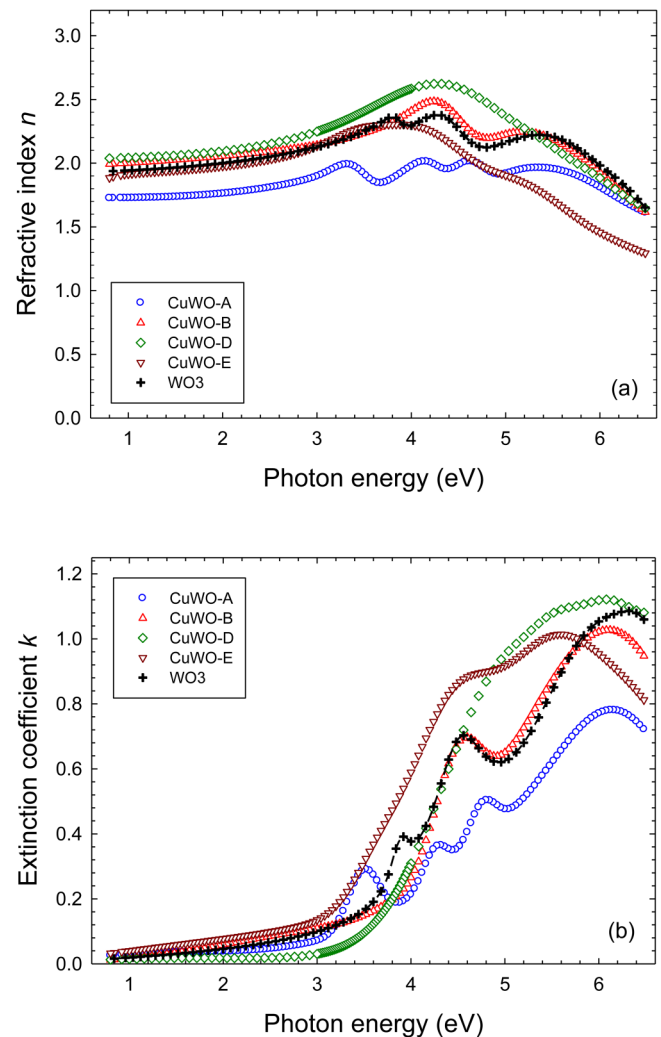


FIG. 11. (a) Refractive index n and (b) extinction coefficient k vs photon energy for annealed Cu_xWO_y films deposited on MG substrates. Also shown are results for a tungsten oxide (WO₃) film.

semi-conductor.^{65,70} In the analysis, we further employ an ellipsometric model taking a gradient of the optical constants throughout the film thickness into account. In this gradient model, the film is divided into several sublayers. Changes of optical constants throughout the sublayers are then calculated with the WVASE software. Figure 12(a) shows the results for two, top and bottom, layers at the surface and near the substrate, respectively, for the CuWO-D film. It is seen that a significant difference between the two layers exists with the bottom layer displaying a somewhat larger absorption above 3.5 eV. The optical (indirect) bandgap energy that can be derived from Fig. 12(a) is about 3.21 eV and the same for both layers (Table IV). We mention in passing that the employed HiPIMS deposition technique with two separate pulses does not cause the noted concentration gradient in the films. This follows immediately if one

24 April 2024 14:10:26

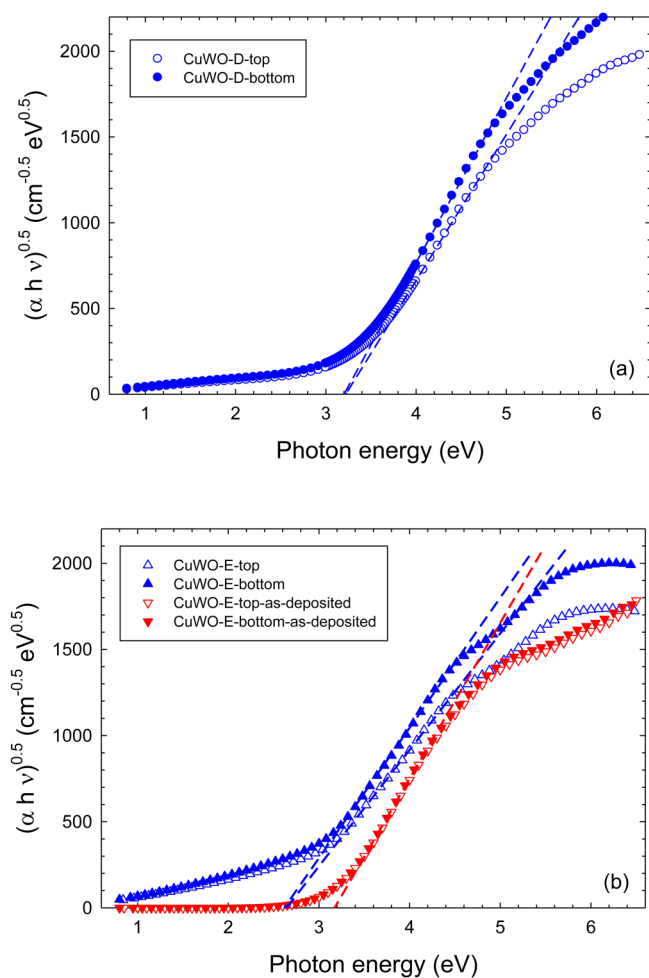


FIG. 12. Tauc plots for (a) an annealed CuWO-D film (\circ , \bullet) and (b) annealed (\triangle , \blacktriangle) and as-deposited (∇ , \blacktriangledown) CuWO-E films on MG substrates. Results for top (open symbols) and bottom (closed symbols) layers are shown (see the text).

considers a typical deposition rate $d/t \approx 5$ nm/min (Table I), which is less than 10^{-3} nm/pulse (at 100 pulses/s). This is considerably smaller than one monolayer per pulse, and therefore, no concentration gradient can develop between the two pulses.

Extracted bandgap energies for all films are summarized in Table IV. The present results for the as-deposited films CuWO-A,

CuWO-B, and CuWO-E are close to the 3.31–3.43 eV of Sun *et al.*⁷⁰ for deposition of WO_3 by pulsed magnetron sputtering. Smaller bandgap energies are extracted for film CuWO-C, which is composed of CuWO_4 , and the annealed CuWO-E film, which contains sodium tungstate. For comparison, bandgap energies extracted from Tauc plots (not shown) assuming a direct bandgap are included in Table IV. In general, extracted direct bandgap energies are significantly larger compared to indirect bandgaps due to the predicted steeper photon energy dependence.

Figure 12(b) displays results for as-deposited and annealed CuWO-E films as obtained from the ellipsometry measurements. It is immediately noted that the plots for the as-deposited and the annealed CuWO-E film differ significantly from each other. The Tauc plot of the annealed film in comparison with the as-deposited film is shifted by ≈ 0.5 eV to smaller photon energies. Optical bandgaps of 3.2 and 2.6 eV for the as-deposited and annealed film are derived from the linear part (dashed line). The smaller bandgap energy of the annealed film in comparison with the CuWO-D film is presumably caused by sodium diffusion into the film during annealing and the formation of sodium tungstate. The results also show that top and bottom sublayers differ significantly for the annealed film, whereas the as-deposited film shows a rather small gradient. As a possible reason, we mention diffusion of Cu atoms during annealing from the surface layers toward the substrate.

D. Electrical and photoelectrical properties

The resistivity of deposited films was measured using the van der Pauw method.⁴¹ We obtain an electrical resistivity of $1.7 \times 10^8 \Omega \text{ cm}$ for the CuWO-E film, which is about $4 \times$ larger compared to a tungsten oxide film deposited under similar conditions. It was not possible to measure the resistivity of the other Cu_xWO_y films, as the resistivity of these films was too large. As a lower limit, we can conclude that the resistivity of the other Cu_xWO_y films was larger than $7 \times 10^9 \Omega \text{ cm}$.

In order to investigate the photoelectrochemical activity for, e.g., water-splitting applications, a photoelectrochemical (PEC) water-splitting functionality study of Cu_xWO_y films was carried out as linear voltammetry experiments. The electrical current was measured as a function of applied voltage (with respect to an Ag/AgCl reference electrode) under simulated solar light irradiation. The scan rate was 10 mV/s. Annealed samples with an area of 1 cm^2 were illuminated for 5 s with a light intensity of 0.62 sun, followed by 5 s without light. In order to check the repeatability, we performed a series of three measurements with the second and third measurement separated by 4 and 68 min from the first measurement. Small differences between the measurements of less than

TABLE IV. Bandgap energy (eV) of films deposited on MG substrates extracted from Tauc plots assuming either indirect or direct bandgaps (BG). For comparison, bandgap energies obtained by extrapolation of the absorption coefficient are also shown.

	CuWO-A	CuWO-B	CuWO-C	CuWO-D	CuWO-E	
	As-deposited	As-deposited	As-deposited	Annealed	As-deposited	Annealed
Indirect BG	3.5	3.5	2.9	3.2	3.2	2.6
Direct BG	3.75	3.7	3.2	4.25	4.1	2.7

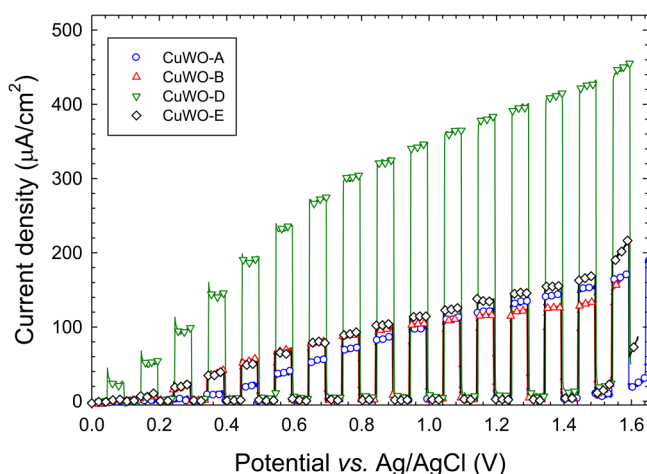


FIG. 13. Current density of annealed Cu_xWO_y films on FTO-coated glass (area 1 cm^2) as a function of applied voltage (vs Ag/AgCl) under simulated solar light irradiation with an intensity of 0.62 sun. Scan rate 10 mV/s , electrolyte $0.1 \text{ mol/l Na}_2\text{SO}_4$, periodically illuminated 5 s dark/5 s light.

2.5% and 5.8%, respectively, were noted (@1 V). The PEC results of several annealed films on FTO-coated glass are displayed in Fig. 13. The measured photocurrent increases with the applied voltage. Typical photocurrent densities at a potential of 1 V are in the range of $105\text{--}135 \mu\text{A}/\text{cm}^2$ (Table I) except for films CuWO-C and CuWO-D. The measured current densities for films CuWO-A, CuWO-B, and CuWO-E are, hence, in fair agreement with recent results for tungsten trioxide.⁶⁵ The CuWO-C film does not show any photoactivity (photocurrent density $<1 \mu\text{A}/\text{cm}^2$). The film has a large Cu/W ratio of more than 2 and, hence, should be dominated by a large copper oxide fraction with p-type photoactivity.⁶⁶ The CuWO-D film shows a photocurrent density of $350 \mu\text{A}/\text{cm}^2$, which is about $3\times$ larger compared to films CuWO-A, CuWO-B, and CuWO-E.

There are at least three reasons that could help to explain the enhanced PEC activity of film CuWO-D compared to the other films. For once, the film was deposited at a gas pressure of 2.4 Pa , and with about 600 nm , it is comparatively thick. Second, according to our GIXRD results, film CuWO-D is partly composed of CuWO_4 (Table III), which is known to have large photoactivity.⁶⁷ Last, film CuWO-D shows a granular and porous surface structure composed of small nano-particles with typical sizes in the range of $20\text{--}40 \text{ nm}$ (Fig. 4) which increases the effective surface area and, thus, could contribute to the enhanced PEC activity of that film.

IV. CONCLUSIONS

Copper tungsten oxide films were deposited with the help of reactive high power impulse magnetron co-sputtering with W and Cu cathodes in an argon/oxygen gas mixture. The film composition depends on the power applied to the Cu cathode keeping the power applied to the W cathode constant. As-deposited and annealed films are examined by various techniques, in particular, EDX, SEM,

GIXRD, Raman spectroscopy, and ellipsometry. GIXRD results show that as-deposited films are x-ray amorphous. Annealed films deposited on MG substrates suffer from sodium diffusion from the glass substrate into the film during annealing. The annealed films with a low Cu content are more affected by Na diffusion compared to films with a larger Cu content. The formation of $\text{Na}_2\text{W}_2\text{O}_7$ and $\text{Na}_2\text{W}_4\text{O}_{13}$ phases is observed. Annealed films with a small Cu content deposited on FTO glass substrates are composed of WO_3 ; films with a larger Cu content contain some admixture of CuWO_4 . Except for film CuWO-C, which has the largest Cu content and a Cu/W ratio of more than 2, it shows the formation of a new monoclinic phase, which is attributed to Cu_2WO_6 formed with monovalent Cu(I) atoms. Raman spectroscopy essentially confirms these findings. The optical bandgap obtained from ellipsometric investigations is about 3.2 eV for as-deposited films and 2.6 eV for the annealed film. The films were also subjected to PEC. Measured photo current densities (at a potential of 1 V vs Ag/AgCl) are in the range of $105\text{--}135 \mu\text{A}/\text{cm}^2$ except for film CuWO-D where this value is $350 \mu\text{A}/\text{cm}^2$. The large photoelectrochemical activity of the CuWO-D film compared to the other films is explained by larger film thickness and a larger CuWO_4 proportion of the film composition.

The present results shed new light on the formation of ternary materials by magnetron co-sputtering. The chosen Cu–W–O material system shows interesting optical and photoelectrochemical properties that could be of interest for sensing, optical, and photocatalytic applications. Future work must focus on depositing films with well-defined stoichiometry and tailoring specific properties for their use.

ACKNOWLEDGMENTS

We would like to thank RNDr. Dagmar Chvostová (Prague) for helpful discussions and her support and Ing. Jan Maňák for his assistance with the SEM analysis. The work was partly supported by the Czech Science Foundation (Project No. 21-04477S), Project Strategy AV21, Program Diagnostic Methods and Techniques, the Czech Academy of Sciences, CzechNanoLab Research Infrastructure project (No. LM2018110), and Project No. SOLID21-CZ.02.1.01/0.0/0.0/16_019/0000760 of the Operational Programme Research, Development and Education financed by European Structural and Investment Funds and the Czech Ministry of Education, Youth and Sports.

AUTHOR DECLARATIONS

Conflict of Interest

The authors have no conflicts to disclose.

Author Contributions

A. Hrubantova: Formal analysis (equal); Investigation (equal); Writing – original draft (equal). **R. Hippler:** Conceptualization (equal); Data curation (equal); Formal analysis (equal); Investigation (equal); Validation (equal); Writing – original draft (equal); Writing – review & editing (equal). **H. Wulff:** Data curation (equal); Formal analysis (equal); Writing – review & editing (equal). **M. Cada:** Data curation (equal); Formal analysis (equal);

Funding acquisition (equal); Writing – review & editing (equal). **O. Gedeon:** Data curation (equal); Formal analysis (equal); Writing – review & editing (equal). **P. Jiricek:** Data curation (equal); Formal analysis (equal); Writing – review & editing (equal). **J. Houdkova:** Data curation (equal); Formal analysis (equal). **J. Olejnick:** Data curation (equal); Formal analysis (equal); Investigation (equal). **N. Nepomniashchaia:** Data curation (equal); Formal analysis (equal); Investigation (equal); Writing – review & editing (equal). **C. A. Helm:** Data curation (equal); Formal analysis (equal). **Z. Hubicka:** Conceptualization (equal); Data curation (equal); Formal analysis (equal); Funding acquisition (equal); Investigation (equal); Project administration (equal); Writing – review & editing (equal).

DATA AVAILABILITY

The data that support the findings of this study are available from the corresponding author upon reasonable request.

REFERENCES

- ¹J. Hirst, S. Müller, D. Peeters, A. Sadlo, L. Mai, O. Mendoza Reyes, D. Friedrich, D. Mitoraj, A. Devi, R. Beranek, and R. Eichberger, “Comparative study of photocarrier dynamics in CVD-deposited CuWO₄, CuO, and WO₃ thin films for photoelectrocatalysis,” *Z. Phys. Chem.* **234**, 699 (2020).
- ²M. M. Arafat, A. S. M. A. Haseeb, and S. A. Akbar, “Developments in semiconducting oxide-based gas-sensing materials,” in *Comprehensive Materials Processing* (Elsevier, 2014), Vol. 13, p. 205.
- ³J. C. Vedrine, “Importance, features and uses of metal oxide catalysts in heterogeneous catalysis,” *Chin. J. Catal.* **40**, 1627 (2019).
- ⁴K. Sivula and R. van de Krol, “Semiconducting materials for photoelectrochemical energy conversion,” *Nat. Rev. Mater.* **1**, 15010 (2016).
- ⁵V. Stranak, M. Cada, M. Quaas, S. Block, R. Bogdanowicz, S. Kment, H. Wulff, Z. Hubicka, C. A. Helm, M. Tichy, and R. Hippler, “Physical properties of homogeneous TiO₂ films prepared by high power impulse magnetron sputtering as a function of crystallographic phase and nanostructure,” *J. Phys. D: Appl. Phys.* **42**, 105204 (2009).
- ⁶C. Dette, M. A. Perez-Osorio, C. S. Kley, P. Punke, C. E. Patrick, P. Jacobson, F. Giustino, S. J. Jung, and K. Kern, “TiO₂ anatase with a bandgap in the visible region,” *Nano Lett.* **14**, 6533 (2014).
- ⁷X. Liu, F. Wang, and Q. Wang, “Nanostructure-based WO₃ photoanodes for photoelectrochemical water splitting,” *Phys. Chem. Chem. Phys.* **14**, 7894 (2012).
- ⁸V. Stranak, Z. Hubicka, M. Cada, R. Bogdanowicz, H. Wulff, C. A. Helm, and R. Hippler, “Influence of reactive oxygen species during deposition of iron oxide films by high power impulse magnetron sputtering,” *J. Phys. D: Appl. Phys.* **51**, 095205 (2018).
- ⁹M. B. Johansson, B. Zietz, G. A. Niklasson, and L. Osterlund, “Optical properties of nanocrystalline WO₃ and WO_{3-x} thin films prepared by DC magnetron sputtering,” *J. Appl. Phys.* **115**, 213510 (2014).
- ¹⁰Z. Jiang, W. Wan, H. Li, S. Yuan, H. Zhao, and P. K. Wong, “A hierarchical Z-scheme α -Fe₂O₃/g-C₃N₄ hybrid for enhanced photocatalytic CO₂ reduction,” *Adv. Mater.* **30**, 1706108 (2018).
- ¹¹W. D. Chemelewski, O. Mabayoje, D. Tang, A. J. E. Rettie, and C. B. Mullins, “Bandgap engineering of Fe₂O₃ with Cr—Application to photoelectrochemical oxidation,” *Phys. Chem. Chem. Phys.* **18**, 1644 (2016).
- ¹²A. Sathé, M. Seki, H. Zhou, J. X. Chen, and H. Tabata, “Bandgap engineering in V-substituted α -Fe₂O₃ photoelectrodes,” *Appl. Phys. Express* **12**, 091003 (2019).
- ¹³A. K. Chawla, S. Singhal, H. O. Gupta, and R. Chandra, “Influence of nitrogen doping on the sputter-deposited WO₃ films,” *Thin Solid Films* **518**, 1430 (2009).
- ¹⁴J. Kleperis, J. Zubkans, and A. R. Lulis, “Nature of fundamental absorption edge of WO₃,” *Proc. SPIE* **2968**, 186 (1997).
- ¹⁵P. P. Gonzalez-Borrero, F. Sato, A. N. Medina, M. L. Baesso, A. C. Bento, G. Baldissera, C. Persson, G. A. Niklasson, C. G. Granqvist, and A. Ferreira da Silva, “Optical band-gap determination of nanostructured WO₃ film,” *Appl. Phys. Lett.* **96**, 061909 (2010).
- ¹⁶A. H. Y. Hendi, M. F. Al-Kuhaili, S. M. A. Durrani, M. M. Faiz, A. Ul-Hamid, A. Qurashi, and I. Khan, “Modulation of the band gap of tungsten oxide thin films through mixing with cadmium telluride towards photovoltaic applications,” *Mater. Res. Bull.* **87**, 148 (2017).
- ¹⁷L. Chen, S. Shet, H. Tang, K.-S. Ahn, H. Wang, Y. Yan, J. Turner, and M. Al-Jassim, “Amorphous copper tungsten oxide with tunable band gaps,” *J. Appl. Phys.* **108**, 043502 (2010).
- ¹⁸Y. Gao and T. W. Hamann, “Quantitative hole collection for photoelectrochemical water oxidation with CuWO₄,” *Chem. Commun.* **53**, 1285 (2017).
- ¹⁹S. Jain, V. K. Varma, A. K. Mahajan, V. H. Khire, and B. Kandasubramanian, “Thermal decomposition of ammonium perchlorate in the presence of copper tungsten oxide (CuWO₄),” *Propellants Explos. Pyrotech.* **46**, 758 (2021).
- ²⁰T. Zhu, M. N. Chong, E. S. Chan, and J. D. Ocon, “Electrochemically-synthesized tungstate nanocomposites γ -WO₃/CuWO₄ and γ -WO₃/NiWO₄ thin films with improved band gap and photoactivity for solar-driven photoelectrochemical water oxidation,” *J. Alloys Compd.* **762**, 90 (2018).
- ²¹N. Gaillard, Y. Chang, A. DeAngelis, S. Higgins, and A. Braun, “A nanocomposite photoelectrode made of 2.2 eV band gap copper tungstate (CuWO₄) and multi-wall carbon nanotubes for solar-assisted water splitting,” *Int. J. Hydrogen Energy* **38**, 3166 (2013).
- ²²T. N. Kol'tsova and G. D. Nipan, “System CuO-WO₃,” *Inorg. Mater.* **35**, 383 (1999).
- ²³B.-O. Mariander, P.-L. Wang, P.-E. Werner, M. Westdahl, A. F. Andresen, and D. Louer, “Powder diffraction studies of Cu₂WO₄,” *Acta Chem. Scand.* **A41**, 152 (1987).
- ²⁴H.-C. Mumm and H. K. Müller-Buschbaum, “Zur Kristallstruktur von Cu₂WO₄,” *J. Less-Common Met.* **142**, 85 (1988).
- ²⁵M. T. Galante, A. Zivkovic, J. C. Alvim, C. C. C. Kleiner, M. Sangali, S. F. R. Taylor, A. J. Greer, C. Hardacre, K. Rajeshwar, R. Caram, R. Bertazzoli, R. T. Macaluso, N. H. de Leeuw, and C. Longo, “Arc synthesis, crystal structure, and photoelectrochemistry of copper(I) tungstate,” *ACS Appl. Mater. Interfaces* **13**, 32865 (2021).
- ²⁶V. Kouznetsov, K. Macak, J. M. Schneider, U. Helmersson, and I. Petrov, *Surf. Coat. Technol.* **122**, 290 (1999).
- ²⁷A. P. Ehiassarian, W.-D. Münz, L. Hultman, U. Helmersson, and I. Petrov, “High power pulsed magnetron sputtered CrN_x films,” *Surf. Coat. Technol.* **163–164**, 267 (2003).
- ²⁸W.-D. Münz, M. Schenkel, S. Kunkel, J. Paulitsch, and K. Bewilogua, “Industrial applications of HIPIMS,” *J. Phys.: Conf. Ser.* **100**, 082001 (2008).
- ²⁹J. Alami, K. Sarakinos, F. Uslu, C. Klever, J. Dukwen, and M. Wuttig, “On the phase formation of titanium oxide films grown by reactive high power pulsed magnetron sputtering,” *J. Phys. D: Appl. Phys.* **42**, 115204 (2009).
- ³⁰A. Anders, “High power impulse magnetron sputtering and related discharges: Scalable plasma sources for plasma-based ion implantation and deposition,” *Surf. Coat. Technol.* **204**, 2864 (2011).
- ³¹J. T. Gudmundsson, D. Lundin, N. Brenning, M. A. Raadu, C. Huo, and T. M. Minea, “An ionization region model of the reactive Ar/O₂ high power impulse magnetron sputtering discharge,” *Plasma Sources Sci. Technol.* **25**, 065004 (2016).
- ³²K. Strijckmans, F. Moens, and D. Depla, “Tutorial: Hysteresis during the reactive magnetron sputtering process,” *J. Appl. Phys.* **124**, 241101 (2018).
- ³³M. Aiempnakit, A. Aijaz, D. Lundin, U. Helmersson, and T. Kubart, “Understanding the discharge current behavior in reactive high power impulse magnetron sputtering of oxides,” *J. Appl. Phys.* **113**, 133302 (2013).
- ³⁴T. Kubart and A. Aijaz, “Evolution of sputtering target surface composition in reactive high power impulse magnetron sputtering,” *J. Appl. Phys.* **121**, 171903 (2017).

- ³⁵Z. Hubicka, M. Zlamal, M. Cada, S. Kment, and J. Krysa, "Photo-electrochemical stability of copper oxide photocathodes deposited by reactive high power impulse magnetron sputtering," *Catal. Today* **328**, 29 (2019).
- ³⁶V. Stranak, Z. Hubicka, P. Adamek, J. Blazek, M. Tichy, P. Spatenka, R. Hippler, and S. Wrehde, "Time-resolved probe diagnostics of pulsed DC magnetron discharge during deposition of TiO_x layers," *Surf. Coat. Technol.* **201**, 2512 (2006).
- ³⁷V. Stranak, M. Quaas, H. Wulff, Z. Hubicka, S. Wrehde, M. Tichy, and R. Hippler, "Formation of TiO_x films produced by high-power pulsed magnetron sputtering," *J. Phys. D: Appl. Phys.* **41**, 055202 (2008).
- ³⁸M. Cada, P. Adamek, V. Stranak, S. Kment, J. Olejnicek, Z. Hubicka, and R. Hippler, "Angle-resolved investigation of ion dynamics in high power impulse magnetron sputtering deposition system," *Thin Solid Films* **549**, 177 (2013).
- ³⁹R. Hippler, Z. Hubicka, M. Cada, P. Ksirova, H. Wulff, C. A. Helm, and V. Stranak, "Angular dependence of plasma parameters and film properties during high power impulse magnetron sputtering for deposition of Ti and TiO₂ layers," *J. Appl. Phys.* **121**, 171906 (2017).
- ⁴⁰R. Hippler, M. Cada, P. Ksirova, J. Olejnicek, P. Jiricek, J. Houdkova, H. Wulff, A. Kruth, C. A. Helm, and Z. Hubicka, "Deposition of cobalt oxide films by reactive pulsed magnetron sputtering," *Surf. Coat. Technol.* **405**, 126590 (2021).
- ⁴¹L. J. van der Pauw, "A method of measuring specific resistivity and Hall effect of discs of arbitrary shape," *Philips Res. Rep.* **13**, 1 (1958); available at https://en.wikipedia.org/wiki/Van_der_Pauw_method.
- ⁴²S. Asgary, M. R. Hantehzadeh, and M. Ghoranneviss, "Temperature dependence of copper diffusion in different thickness amorphous tungsten/tungsten nitride layer," *Phys. Met. Metallogr.* **118**, 1127 (2017).
- ⁴³M. Moriyama and M. Kajihara, "Fast penetration of Cu in Ni of Cu/Ni/Cu diffusion couples due to diffusion induced recrystallization," *ISIJ Int.* **38**, 489 (1998).
- ⁴⁴K. Kanaya and S. Okayama, "Penetration and energy-loss theory of electrons in solid targets," *J. Phys. D: Appl. Phys.* **5**, 43 (1972).
- ⁴⁵Y. Tang, N. Rong, F. Liu, M. Chu, H. Dong, Y. Zhang, and P. Xiao, "Enhancement of the photoelectrochemical performance of CuWO₄ films for water splitting by hydrogen treatment," *Appl. Surf. Sci.* **361**, 133 (2016).
- ⁴⁶M. C. Biesinger, "Advanced analysis of copper X-ray photoelectron spectra," *Surf. Interface Anal.* **49**, 1325 (2017).
- ⁴⁷A. K. Mukhopadhyay, A. Roy, G. Bhattacharjee, S. C. Das, A. Majumdar, H. Wulff, and R. Hippler, "Surface stoichiometry and depth profile of Ti_x-Cu_yN_z thin films deposited by magnetron sputtering," *Materials* **14**, 3191 (2021).
- ⁴⁸X. Dong, Z. Wu, Y. Guo, Y. Tong, X. Liu, L. Zhang, and Y. Lu, "Rational modification in the photochromic and self-bleaching performance of hierarchical microsphere Cu@h-WO₃/WO₃·nH₂O composites," *Sol. Energy Mater. Sol. Cells* **219**, 110784 (2021).
- ⁴⁹T. Abe, H. Hamatani, S. Higashide, M. Hara, and S. Akamaru, "Surface coating of small SiO₂ particles with a WO₃ thin film by barrel-sputtering method," *J. Alloys Compd.* **441**, 157 (2007).
- ⁵⁰C. Santato, M. Odziemkowski, M. Ulmann, and J. Augustynski, "Crystallographically oriented mesoporous WO₃ films: Synthesis, characterization, and applications," *J. Am. Chem. Soc.* **123**, 10639 (2001).
- ⁵¹F. D. Hardcastle and I. E. Wachs, "Determination of the molecular structures of tungstates by Raman spectroscopy," *J. Raman Spectrosc.* **26**, 397 (1995).
- ⁵²J. Ruiz-Fuertes, D. Errandonea, R. Lacomba-Perales, A. Segura, J. Gonzalez, F. Rodriguez, F. J. Manjon, S. Ray, P. Rodriguez-Hernandez, A. Munoz, Z. Zhu, and C. Y. Tu, "High-pressure structural phase transitions in CuWO₄," *Phys. Rev. B* **81**, 224115 (2010).
- ⁵³W. Thongpan, D. Louloudakis, P. Pooseekheaw, T. Kumpika, E. Kantarak, W. Sroil, A. Panthawan, W. Thongsuwan, and P. Singjai, "Porous CuWO₄/WO₃ composite films with improved electrochromic properties prepared by sparking method," *Mater. Lett.* **257**, 126747 (2019).
- ⁵⁴V. S. Levitskii, V. I. Shapovalov, A. E. Komlev, A. V. Zav'yalov, V. V. Vit'ko, A. A. Komlev, and E. S. Shutova, "Raman spectroscopy of copper oxide films deposited by reactive magnetron sputtering," *Tech. Phys. Lett.* **41**, 1094 (2015).
- ⁵⁵A. Boulett, G. Del C. Pizarro, R. Martin-Trasanco, J. Sanchez, F. Tasca, O. E. Linarez Perez, A. Tello, and D. P. Oyarzun, "Electrodeposition of Cu₂O nanostructures with improved semiconductor properties," *Cogent Eng.* **8**, 1875534 (2021).
- ⁵⁶M. Wang, J. Cheng, M. Li, and F. He, "Raman spectra of soda-lime-silicate glass doped with rare earth," *Physica B* **406**, 3865 (2011).
- ⁵⁷J. Wang, J. L. You, A. A. Sobol, L. M. Lu, M. Wang, J. Wu, X. M. Lv, and S. M. Wan, "In-situ high temperature Raman spectroscopic study on the structural evolution of Na₂W₂O₇ from the crystalline to molten states," *J. Raman Spectrosc.* **48**, 298 (2017).
- ⁵⁸F. Knee and R. A. Condrate, Sr., "The Raman spectrum of sodium ditungstate Na₂W₂O₇," *J. Phys. Chem. Solids* **40**, 1145 (1979).
- ⁵⁹T. Caruso, M. Castriota, A. Policicchio, A. Fasanella, M. P. De Santo, F. Ciuchi, G. Desiderio, S. La Rosa, P. Rudolf, R. G. Agostino, and E. Cazzanelli, "Thermally induced evolution of sol-gel grown WO₃ films on ITO/glass substrates," *Appl. Surf. Sci.* **297**, 195 (2014).
- ⁶⁰C.-Y. Kim, S.-H. Huh, and D.-H. Riu, "Formation of nano-rod sodium tungstate film by sodium ion diffusion," *Mater. Chem. Phys.* **116**, 527 (2009).
- ⁶¹K. Viswanathan, "Crystal structure of sodium tetratungstate, Na₂W₄O₁₃," *J. Chem. Soc., Dalton Trans.* (20), 2170 (1974).
- ⁶²P. Yadav and E. Sinha, "Structural and optical properties of triclinic CuWO₄ prepared by solid-state reaction technique," *Macromol. Symp.* **388**, 1900019 (2019).
- ⁶³C. M. Tian, M. Jiang, D. Tang, L. Qiao, H. Y. Xiao, B. F. E. Oropeza, J. P. Hofmann, E. J. M. Hensen, A. Tadich, W. Li, D. C. Qig, and K. H. L. Zhang, "Elucidating the electronic structure of CuWO₄ thin films for enhanced photoelectrochemical water splitting," *J. Mater. Chem. A* **7**, 11895 (2019).
- ⁶⁴J. Tauc, R. Grigorovic, and A. Vancu, "Optical properties and electronic structure of amorphous germanium," *Phys. Stat. Sol.* **15**, 627 (1966).
- ⁶⁵J. Olejnicek, A. Hrubantova, L. Volfova, M. Dvorakova, M. Kohout, D. Tvarog, O. Gedeon, H. Wulff, R. Hippler, and Z. Hubicka, "WO₃ and WO_{3-x} thin films prepared by DC hollow cathode discharge," *Vacuum* **195**, 110679 (2022).
- ⁶⁶M. Izaki, M. Nagai, K. Maeda, F. B. Mohamad, K. Motomura, J. Sasano, T. Shinagawa, and S. Watase, "Electrodeposition of 1.4-eV-bandgap p-copper (II) oxide film with excellent photoactivity," *J. Electrochem. Soc.* **158**, D578 (2011).
- ⁶⁷B. Peng, C. Li, C. Yue, and P. Diao, "Sacrificial template synthesis of copper tungstate: Influence of preparing conditions on morphology and photoactivity," *Int. J. Electrochem. Sci.* **14**, 2574 (2019).
- ⁶⁸A. Anders, "A structure zone diagram including plasma-based deposition and ion etching," *Thin Solid Films* **518**, 4087 (2010).
- ⁶⁹R. Hippler, M. Cada, V. Stranak, C. A. Helm, and Z. Hubicka, *J. Appl. Phys.* **125**, 013301 (2019).
- ⁷⁰X. Sun, Z. Liu, and H. Cao, "Effects of film density on electrochromic tungsten oxide thin films deposited by reactive dc-pulsed magnetron sputtering," *J. Alloys Compd.* **504**, S418 (2010).